



## PAPER

## OPEN ACCESS

RECEIVED  
4 February 2023REVISED  
16 March 2023ACCEPTED FOR PUBLICATION  
23 March 2023PUBLISHED  
12 April 2023

Original Content from  
this work may be used  
under the terms of the  
[Creative Commons  
Attribution 4.0 licence](#).

Any further distribution  
of this work must  
maintain attribution to  
the author(s) and the title  
of the work, journal  
citation and DOI.



# Improving barocaloric properties by tailoring transition hysteresis in $\text{Mn}_3\text{Cu}_{1-x}\text{Sn}_x\text{N}$ antiperovskites

Frederic Rendell-Bhatti<sup>1,5</sup> , Ming Zeng<sup>2,5</sup> , Pol Lloveras<sup>2</sup> , Josep-Lluís Tamarit<sup>2</sup> , María Barrio<sup>2</sup> , Eamonn T Connolly<sup>3</sup> , Donald A MacLaren<sup>1</sup> , Freya Johnson<sup>4</sup> , Lesley F Cohen<sup>4</sup> and David Boldrin<sup>1,\*</sup>

<sup>1</sup> SUPA, School of Physics and Astronomy, University of Glasgow, Glasgow G12 8QQ, United Kingdom

<sup>2</sup> Departament de Física, EEBE, Campus Diagonal-Besòs and Barcelona Research Center in Multiscale Science and Engineering, Universitat Politècnica de Catalunya, Eduard Maristany, 10-14, 08019 Barcelona, Catalonia, Spain

<sup>3</sup> Diamond Light Source Ltd, Diamond House, Harwell Science and Innovation Campus, Didcot, Oxfordshire, OX11 0DE, United Kingdom

<sup>4</sup> Department of Physics, Blackett Laboratory, Imperial College London, London SW7 2AZ, United Kingdom

<sup>5</sup> These two authors contributed equally.

\* Author to whom any correspondence should be addressed.

E-mail: [david.boldrin@glasgow.ac.uk](mailto:david.boldrin@glasgow.ac.uk)

**Keywords:** barocalorics, first order phase transitions, entropy

Supplementary material for this article is available [online](#)

## Abstract

The magnetically frustrated manganese nitride antiperovskite family displays significant changes of entropy under changes in hydrostatic pressure near a first-order antiferromagnetic to paramagnetic phase transition that can be useful for the emerging field of solid-state barocaloric cooling. In previous studies, the transition hysteresis has significantly reduced the reversible barocaloric effects (BCE). Here we show that the transition hysteresis can be tailored through quaternary alloying in the  $\text{Mn}_3\text{Cu}_{1-x}\text{Sn}_x\text{N}$  system. We find the magnitude of hysteresis is minimised when Cu and Sn are equiatomic ( $x = 0.5$ ) reaching values far less than previously found for  $\text{Mn}_3\text{AN}$  ( $A = \text{Pd}, \text{Ni}, \text{Ga}, \text{Zn}$ ), whilst retaining entropy changes of the same order of magnitude. These results demonstrate that reversible BCE are achievable for  $p < 100$  MPa in the  $\text{Mn}_3(A, B)\text{N}$  family and suggest routes to modify the transition properties in compounds of the same family.

## 1. Introduction

Barocalorics are emerging as a potential competitor to conventional vapour-compression-based heating and cooling technologies, such as heat pumps, refrigerators and air conditioners. They offer opportunities for greater energy-efficiency without the need for environmentally harmful fluids with high global warming potential. This emerging field has been driven by an ever-increasing catalogue of materials that demonstrate entropy changes with magnitudes comparable to those used in vapour-compression systems [1–4]. However, device engineering challenges have limited the industrial feasibility of this technology due to large pressures required ( $p > 100$  MPa).

This drawback is due to significant transition hysteresis, intrinsic to the first-order phase transitions of many barocaloric materials. As such, understanding and manipulating hysteresis in such materials remains a key challenge.

Although metallic systems display smaller barocaloric effects (BCE) compared to some other barocaloric families, they may combine giant BCE, large thermal conductivity, low thermal hysteresis, tunable transition temperatures and high density. Notable examples of metallic barocalorics include Heusler alloys [5–9], MnCoGe-type alloys [9, 10] and, the focus of this study, manganese nitride antiperovskites ( $\text{Mn}_3\text{AN}$ , where in this case  $A = \text{Ga}$  and  $\text{Ni}$ ) [11, 12]. The latter have received a resurgence of interest due to the variety of unusual functional properties they display, such as an anomalous coefficient of resistivity [13], negative thermal expansion [14], and piezomagnetism [12]. It should be noted here that the  $\text{Mn}_3\text{AN}$  family of materials demonstrate an inverse BCE [15], such that  $\Delta S$  increases with increasing  $p$ . This is in contrast to

the conventional BCE, which is characterised by a decrease in  $\Delta S$  with increasing  $p$ . Recently, giant inverse BCE (hereafter simply referred to as BCE) have been reported in the  $A = \text{Ga}$  and  $\text{Ni}$  members of the family [11, 12]. These effects originate from a non-collinear antiferromagnetic (AFM) order born from frustrated spin interactions, which strengthen with changes of volume and via feedback with the underlying electronic structure as magnetic order develops [12]. Coupling between magnetovolume effects and electronic structure leads to a complex and rich mechanism that underpins the strongly first-order AFM to paramagnetic transition and, hence, the giant BCE [12].

Alloying multiple elements onto the  $A$ -site of the  $\text{Mn}_3\text{AN}$  family has previously been used as a method to tune their functional properties [14, 16, 17]. Our recent efforts have gone towards tailoring the BCE in  $\text{Mn}_3(A,B)\text{N}$  to room temperature whilst maintaining large isothermal entropy changes [18]. Our atmospheric pressure measurements on a sample of  $\text{Mn}_3\text{Zn}_{0.5}\text{In}_{0.5}\text{N}$  suggested that the transition hysteresis was  $< 2$  K, however it did not translate to a large reversible barocaloric entropy change. Here we focus on the antiperovskite series  $\text{Mn}_3\text{Cu}_{1-x}\text{Sn}_x\text{N}$ , which has previously been studied in relation to its anomalous thermal expansion [14]. Interestingly, for this series the  $x = 0$  and  $x = 1$  members go through magnetic transitions with zero concomitant volume change and therefore, no BCE associated with the transition will occur. However, Takenaka *et al* [14] showed that for  $0.1 < x < 0.7$  it is possible to induce a large volume change at the magnetic transition, which is a prerequisite for the BCE. Here we show that (i) large BCE are indeed found in  $\text{Mn}_3\text{Cu}_{1-x}\text{Sn}_x\text{N}$  and (ii) the hysteresis of the transition is significantly reduced in comparison to  $\text{Mn}_3\text{AN}$ . For the latter, and in contrast to  $\text{Mn}_3\text{AN}$ , we show that the hysteresis is independent of the transitional volume change. This suggests that it may be due to an extrinsic effect and it may therefore be possible to further reduce hysteresis in these materials without compromising the BCE. Taken together, our results show that reversible entropy changes are possible in metallic barocaloric systems at  $p < 100$  MPa.

## 2. Experimental

Samples were synthesised using the general procedure previously reported [12, 18].  $\text{Mn}_3\text{CuN}$  and  $\text{Mn}_3\text{SnN}$  were individually prepared and then mixed together in the required ratios to form  $\text{Mn}_3\text{Cu}_{1-x}\text{Sn}_x\text{N}$ . This final reaction step was performed twice at 1053 K for 40 h with intermediate grindings.

Powder synchrotron diffraction data was collected on the I11 beamline (Diamond Light Source, UK) with  $E = 15$  keV ( $\lambda = 0.826755$  Å) synchrotron radiation. Data were collected using a 0.3 mm borosilicate capillary to minimise absorption effects ( $\mu R \sim 0.3$ ). Temperature-dependent data were collected under continuous heating using the Oxford Cryosystems' 800 Series Cryosteam Plus. Samples were heated at  $1$  K  $\text{min}^{-1}$  while 2 s scans were collected continuously using the position sensitive Dectris Mythen2 detector. Data analysis was performed using GSAS2 [19]. Rietveld refinements were performed using two antiperovskite phases, due to the phase coexistence region, with the phase fraction of each allowed to refine freely and the sum of both set to unity.

Differential scanning calorimetry (DSC) at atmospheric pressure was carried out with a DSC Q100 (TA Instruments). A few tenths of a mg of ground samples were encapsulated in sealed aluminium pans. Ramps on heating and cooling across the first-order phase transition were performed at different rates in the range  $2$ – $10$  K  $\text{min}^{-1}$ . Heat capacity data were collected on a 3.09 mg sample using the heat capacity option on a quantum design physical property measurement system, performed isothermally with a temperature rise of 2%, and can be found in figure S1. The sample was fixed to the platform using thermal conductive grease (Apiezon N Grease). The heat capacity of the puck and grease were measured separately as an addenda and were subtracted from the total measured data to obtain the sample heat capacity.

Temperature-dependent calorimetry was performed using a MV1-30 high-pressure cell (Unipress, Poland) adapted as a thermal analyser, and operating from atmospheric pressure to 0.6 GPa and within a temperature range from 205 K up to 393 K. Ceramic samples were directly attached to Peltier modules acting as thermal sensors. Heating and cooling ramps were performed at  $\sim 2$  K  $\text{min}^{-1}$  using an external thermal jacket attached to a thermal bath (Lauda Proline RP1290). The pressure-transmitting fluid was DW-Therm M90.200.02 (Huber). Calculations of the entropy curves are detailed in the SI.

Magnetic susceptibility data were collected using a quantum design MPMS-3 magnetometer. Temperature-dependent data were collected with varying ramp rates between 1 and 10 K  $\text{min}^{-1}$ , under an applied field of 0.05 T.

Scanning electron microscopy combined with electron backscatter diffraction (EBSD) and X-ray energy dispersive spectroscopy (EDS) were performed in a Thermo-Fisher Helios G4 dual-beam Xe plasma focussed ion beam instrument. Sintered pellets were polished using wet sandpaper and then finished with  $5$   $\mu\text{m}$   $\text{Al}_2\text{O}_3$  suspensions on a polishing cloth.

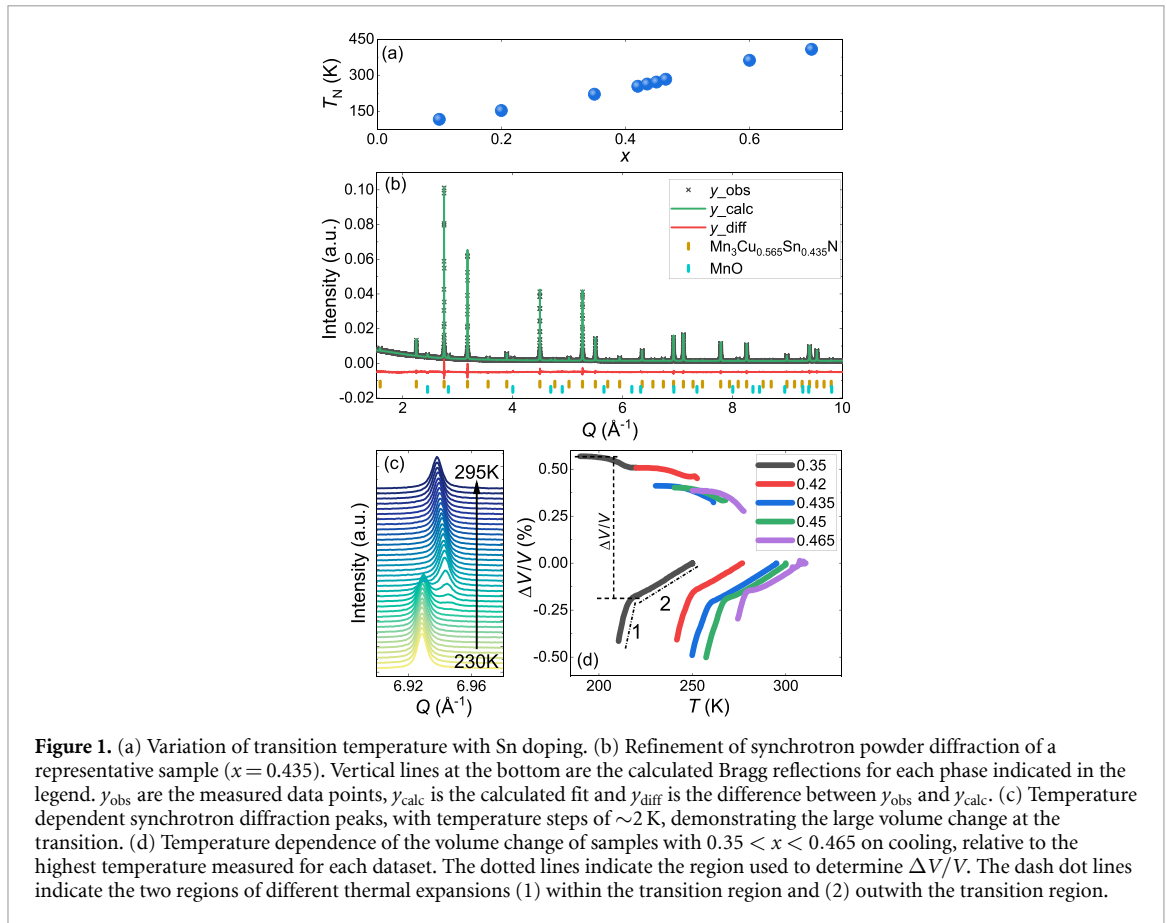


**Figure 1.** (a) Variation of transition temperature with Sn doping. (b) Refinement of synchrotron powder diffraction of a representative sample ( $x = 0.435$ ). Vertical lines at the bottom are the calculated Bragg reflections for each phase indicated in the legend.  $y_{\text{obs}}$  are the measured data points,  $y_{\text{calc}}$  is the calculated fit and  $y_{\text{diff}}$  is the difference between  $y_{\text{obs}}$  and  $y_{\text{calc}}$ . (c) Temperature dependent synchrotron diffraction peaks, with temperature steps of  $\sim 2$  K, demonstrating the large volume change at the transition. (d) Temperature dependence of the volume change of samples with  $0.35 < x < 0.465$  on cooling, relative to the highest temperature measured for each dataset. The dotted lines indicate the region used to determine  $\Delta V/V$ . The dash dot lines indicate the two regions of different thermal expansions (1) within the transition region and (2) outwith the transition region.

### 3. Results and discussion

Our study involves samples of  $\text{Mn}_3\text{Cu}_{1-x}\text{Sn}_x\text{N}$  with a range of  $x$  values between 0.1 and 0.7, however the majority of our data were collected on samples with  $0.35 < x < 0.465$  where the paramagnetic to AFM transition temperature,  $T_N$ , lies close to room temperature or below. Our results are structured into three parts: (i) characterisation at atmospheric pressure, (ii) determination of the BCE and (iii) discussion.

#### 3.1. Characterisation at atmospheric pressure

The variation of the transition temperature as a function of  $x$ , determined using either magnetometry, DSC or X-ray diffraction, is shown in figure 1(a) and is in excellent agreement with previously reported data [14].

Lab-based x-ray diffraction confirmed the presence of Bragg reflections consistent with the antiperovskite structure for all samples, with a minority phase of MnO that is challenging to eliminate in these materials. Further analysis of the crystal structure was performed for  $0.35 < x < 0.465$  using powder synchrotron diffraction as a function of temperature. A typical diffractogram and Rietveld refinement is shown in figure 1(b) for the sample  $x = 0.435$ . An excellent fit is achieved with the expected antiperovskite structure ( $Pm\bar{3}m$ , Cu/Sn Wyckoff 1a, N 1b and Mn 3c) and the refined fractional occupancies of Sn and Cu were close to the nominal values for all samples (see table S1 in the SI).

Synchrotron data were collected as a function of temperature in order to determine the relative volume change,  $\Delta V/V$ , for each sample. A typical thermodiffractogram is shown in figure 1(c), demonstrating a phase transition with a large peak position shift and a phase coexistence region where two clear peaks are evident. The refined volume change,  $\Delta V/V$ , for all measured samples is shown in figure 1(d). All samples demonstrate similar temperature dependence with  $0.5 < \Delta V/V < 0.7\%$  at the PM-AFM transition. However, it is clear that the transitional volume change decreases with increasing  $x$  (see table 1), as expected from previous results [14]. A remarkable observation from this plot is that the paramagnetic phase of all samples shows a significantly enhanced thermal expansion in the phase coexistence region (see dash dot lines in figure 1(d)). We had observed signs of similar behaviour in the material  $\text{Mn}_3\text{Zn}_{0.5}\text{In}_{0.5}\text{N}$ , although it was inconclusive [18]. Here, the behaviour is much clearer although its origin remains an open question.

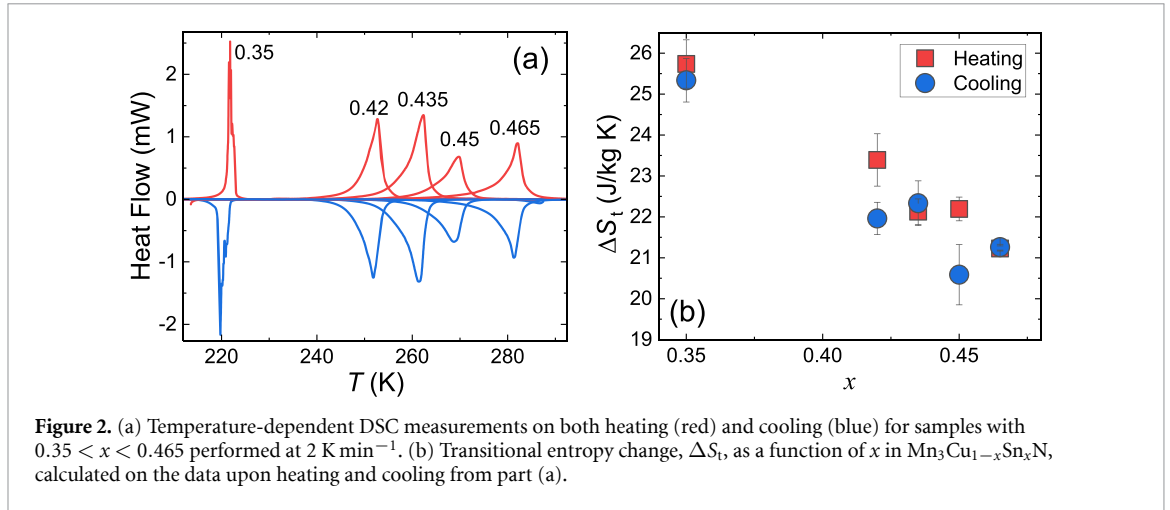


**Figure 2.** (a) Temperature-dependent DSC measurements on both heating (red) and cooling (blue) for samples with  $0.35 < x < 0.465$  performed at  $2 \text{ K min}^{-1}$ . (b) Transitional entropy change,  $\Delta S_t$ , as a function of  $x$  in  $\text{Mn}_3\text{Cu}_{1-x}\text{Sn}_x\text{N}$ , calculated on the data upon heating and cooling from part (a).

**Table 1.** Properties relevant to the barocaloric effects of Mn antiperovskites and other metallic barocaloric systems. For the latter, where a number of related materials exist, the member with the lowest hysteresis is shown here. Transition temperature,  $T_t$ ; relative transitional volume change,  $\Delta V/V$ ; sensitivity of the transition to pressure,  $\frac{dT_t}{dp}$ ; thermal hysteresis of materials studied in this work were determined as described in the text,  $\Delta T_{\text{hys}}$ ; transitional entropy change,  $\Delta S_t$ ; minimum reversible pressure calculated from the  $(T, p)$  phase diagram,  $p_{\text{rev}}$ , as the value for which the endothermic transition temperature is equal to the exothermic transition temperature at atmospheric pressure. Values of  $p_{\text{rev}}$  in parenthesis were estimated from  $p_{\text{rev}} = \Delta T_{\text{hys}} (dT/dp)^{-1}$  according to [20].

	$T_t$ (K)	$ \Delta V/V $ (%)	$\frac{dT_t}{dp}$ (K GPa $^{-1}$ )	$\Delta T_{\text{hys}}$ (K)	$ \Delta S_t $ (J K $^{-1}$ kg $^{-1}$ )	$p_{\text{rev}}$ (MPa)	References
$\text{Mn}_3\text{NiN}$	262	0.40	13.5	4	52	600	[12]
$\text{Mn}_3\text{GaN}$	290	1.00	-65	6	22	(92)	[11]
$\text{Mn}_3\text{ZnN}$	180	1.50	-70	8	39	(114)	[14, 18, 21]
$\text{Mn}_3\text{PdN}$	290	0.20	-14	2	30	150	[22]
$\text{Mn}_3\text{Zn}_{0.5}\text{In}_{0.5}\text{N}$	300	0.9	-33	1	37	240	[18]
$\text{Mn}_3\text{Cu}_{0.65}\text{Sn}_{0.35}\text{N}$	220	0.75	-42	1.3	25	40	This work
$\text{Mn}_3\text{Cu}_{0.58}\text{Sn}_{0.42}\text{N}$	253	0.65	-40	0.5	22	20	This work
$\text{Mn}_3\text{Cu}_{0.565}\text{Sn}_{0.435}\text{N}$	262	0.62	-39	0.5	22	20	This work
$\text{Mn}_3\text{Cu}_{0.55}\text{Sn}_{0.45}\text{N}$	271	0.60	-37	0.3	22	50	This work
$\text{Mn}_3\text{Cu}_{0.535}\text{Sn}_{0.465}\text{N}$	283	0.55	-37	0.4	21	80	This work
$\text{Ni}_{0.85}\text{Fe}_{0.15}\text{S}$	303	1.6	-75	11.5	53	(153)	[23]
$\text{MnNiSi}_{0.61}\text{FeCoGe}_{0.39}$	311	2.7	-70	4	63	175	[24]
$\text{MnCoGe}_{0.99}\text{In}_{0.01}$	310	4.4	-77	8	52	(104)	[25]
$\text{Fe}_{49}\text{Rh}_{51}$	310	1	60	10	12	150	[26]
$\text{Ni}_{35.5}\text{Co}_{14.5}\text{Mn}_{35}\text{Ti}_{15}$	249	1.6	58	7	40	>100	[27]
$\text{Ni}_{1.99}\text{Mn}_{1.37}\text{In}_{0.64}$	329	0.6	19.5	4	40	>250	[7]
$\text{La}_{1.2}\text{Ce}_{0.8}\text{Fe}_{11}\text{Si}_2\text{H}_{1.86}$	310	1.7	-260	$\sim 1$	—	50	[28]

Atmospheric pressure DSC measurements were performed to investigate the entropy changes at the magnetic transition across the series. The DSC data, as a function of temperature, for samples  $0.35 < x < 0.465$  are shown in figure 2(a). The transition becomes broader with increasing  $x$ , particularly for  $x > 0.35$ , indicating increased phase coexistence in these samples. The measured transitional entropy change,  $\Delta S_t$ , as a function of  $x$  is shown in figure 2(b). The trend of decreasing  $\Delta S_t$  with increasing  $x$  is perhaps expected based on both (i) the increased transition temperature and (ii) the observed trends in both  $\Delta V/V$  and the width of the DSC peak in figure 2(a). Nonetheless, the changes in  $\Delta S_t$  are only 10%–20% across this range of samples, and the absolute value of  $\Delta S_t$  for the  $x = 0.465$  sample is very similar to that found in  $\text{Mn}_3\text{GaN}$  ( $\Delta S_t = 22 \text{ J kg}^{-1} \text{ K}^{-1}$ , see table 1).

For all samples, a striking feature of the DSC data in figure 2(a) is the remarkably small hysteresis of the transition. Measurement of the hysteresis was performed by taking data at different temperature ramp rates between 0.5 and  $10 \text{ K min}^{-1}$ . A linear fit to these datasets allowed extrapolation of the hysteresis to  $0 \text{ K min}^{-1}$  (see figure S8). All samples have an extrapolated hysteresis of  $\Delta T_{\text{hys}} < 1.5 \text{ K}$ , with most samples having a hysteresis of  $\sim 0.5 \text{ K}$ . It is noteworthy that the transition temperature has a weak and linear dependence on the ramp rate (see SI figure S8) which indicates that the transition has a significant athermal character [29]. This is in stark contrast to the plastic crystal neopentyl glycol, which has recently been characterised as a promising barocaloric material [3]. Organic plastic crystals and other barocaloric pure

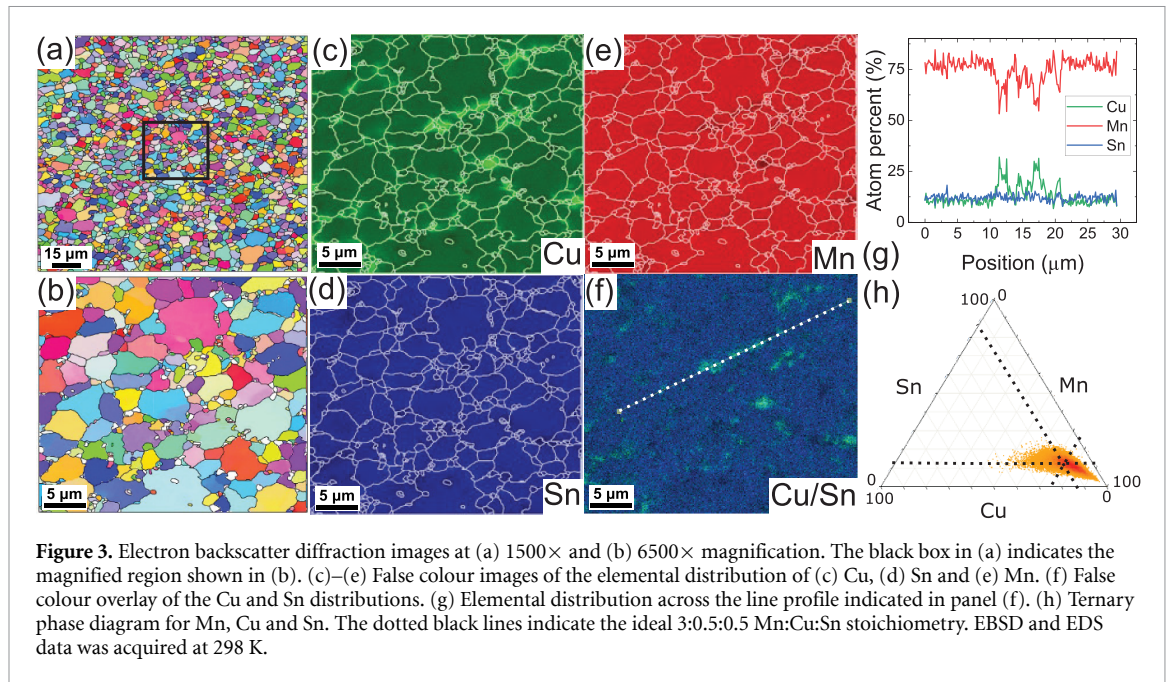


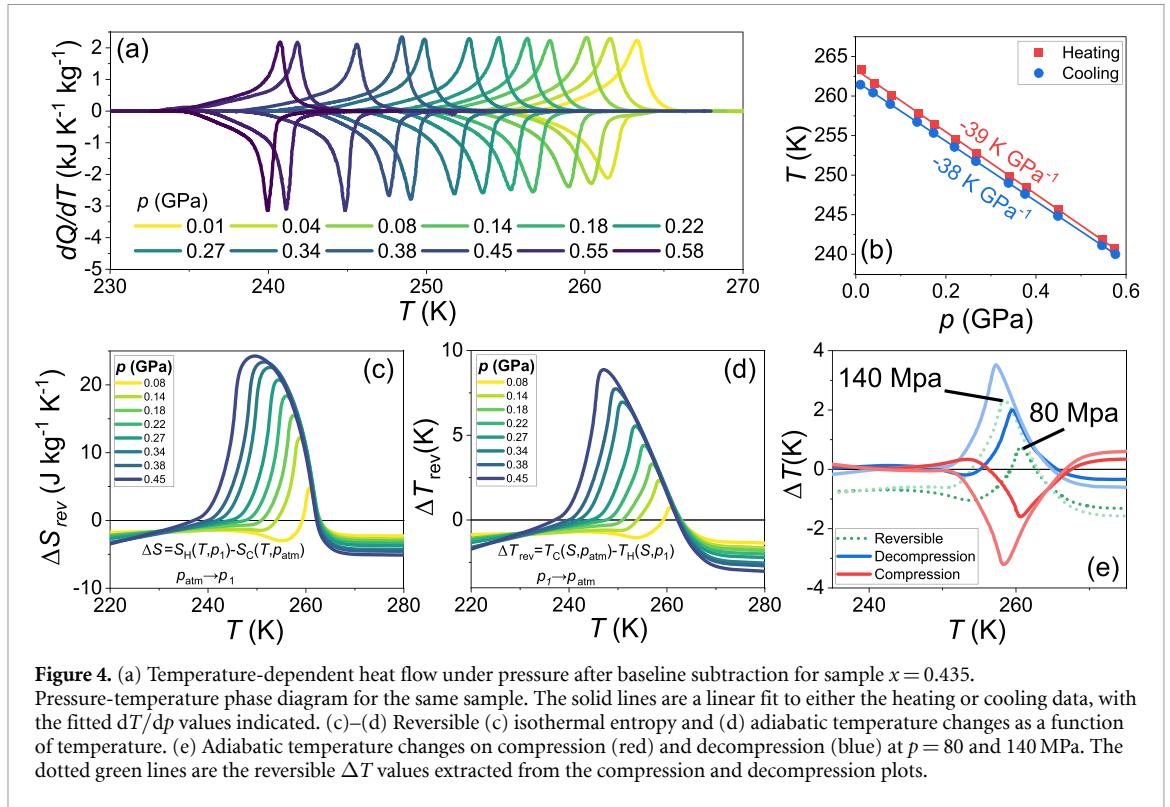
**Figure 3.** Electron backscatter diffraction images at (a) 1500 $\times$  and (b) 6500 $\times$  magnification. The black box in (a) indicates the magnified region shown in (b). (c)–(e) False colour images of the elemental distribution of (c) Cu, (d) Sn and (e) Mn. (f) False colour overlay of the Cu and Sn distributions. (g) Elemental distribution across the line profile indicated in panel (f). (h) Ternary phase diagram for Mn, Cu and Sn. The dotted black lines indicate the ideal 3:0.5:0.5 Mn:Cu:Sn stoichiometry. EBSD and EDS data was acquired at 298 K.

compounds in general show significant isothermal character with a strong dependence of both the peak maximum temperature and peak width on the ramp rate.

To further characterise the samples at a microstructural level we performed EBSD along with EDS on a mechanically polished sample of  $\text{Mn}_3\text{Cu}_{0.5}\text{Sn}_{0.5}\text{N}$  ( $x = 0.5$ ). An EBSD image with a horizontal field width of  $\sim 100 \mu\text{m}$  captured over 1800 grains (see figure 3(a)) with a mean grain size of  $\sim 4 \mu\text{m}$ , demonstrating that particle sizes were relatively large and disordering due to nanostructural effects can be ruled out. EDS data collected across this whole region gives a Mn:(Cu,Sn) ratio of 2.98:1 and a ratio of Cu:Sn of 1.05:1, demonstrating an excellent agreement to the nominal  $\text{Mn}_3\text{Cu}_{0.5}\text{Sn}_{0.5}\text{N}$  composition ( $N$  peaks in EDS lie at too low energy for reliable quantification). EDS data collected on a reduced region of  $\sim 100$  grains are shown in figures 3(b)–(f). The element with most variation across this region is Cu. From the colour scale in figure 3(c), it is clear that this variation occurs only in small regions ( $< 5 \mu\text{m}$ ), localised between the larger antiperovskite grains. This is further demonstrated by the elemental variation line profile indicated in figure 3(f), which is plotted in figure 3(g). Here one can see that increase in Cu across the regions of smaller grains coincides with a decrease in Mn and little change in Sn; we propose that this is caused by a very small percentage of a separate third phase. The same line profile at the centre of the larger grains shows the expected 3:0.5:0.5 Mn:Cu:Sn ratio within error expected of the antiperovskite phase. Finally, a ternary phase diagram of Mn/Cu/Sn from the EDS data presented is shown in figure 3(h). Here one can see that the distribution of the stoichiometry is centred quite closely on the expected 3:0.5:0.5 Mn:Cu:Sn ratio. The slightly larger distribution in the Mn concentration is due to the presence of MnO particles. Taken together, the EBSD and EDS analyses demonstrate that the stoichiometry is close to that expected and that inhomogeneity in the Cu and Sn mixing between grains is not the cause of the low hysteresis.

### 3.2. Determination of the BCE

We now turn to pressure dependent heat flow measurements in order to explore the BCE. Measurements were performed for samples with  $0.35 < x < 0.465$ . Representative datasets for sample  $x = 0.435$  are shown in figure 4. The remaining datasets are included in figure S3 and extracted parameters for all samples are provided in table 1. The background subtracted heat flow measurements are plotted in figure 4(a) for applied pressures  $0 < p$  (GPa)  $< 0.6$ . From these data we can plot the pressure–temperature phase diagram, figure 4(b), which (i) shows that the small hysteresis is maintained at high pressure due to the similarity of  $\frac{dT}{dp}$  for endothermic and exothermic transitions and (ii) allows us to calculate the sensitivity of the transition,  $\frac{dT}{dp} \sim -39 \text{ K GPa}^{-1}$ . Extracted from the data in figure 4(a) with the method explained in the SI, the entropy plotted as a function of temperature on cooling and heating is shown in SI figure S4 (see figure S5 for all analysed samples). Finally, using quasi-direct methods [3], we calculate the associated barocaloric isothermal entropy change,  $\Delta S$ , and adiabatic temperature changes,  $\Delta T$ . For each sample these values are plotted in SI figures S6 and S7.



The reversible BCEs are summarised in figures 4(c)–(e). It can be noted that  $\Delta S_{\text{rev}}$  below the transition is very small (consistent with the nearly inverse behaviour in this temperature interval),  $\Delta S_{\text{rev}}$  across the transition is positive upon compression (consistent with the inverse effects due to  $\frac{dT}{dp} < 0$ ) and  $\Delta S_{\text{rev}}$  above the transition is negative upon compression (consistent with the positive thermal expansion of the high-temperature phase). In turn,  $\Delta T_{\text{rev}}$  is displayed in figure 4(d) for decompression processes, for which it shows the same sign as  $\Delta S_{\text{rev}}$ . Whilst the magnitudes of the BCEs are similar to previously reported values for Mn antiperovskites [11, 12, 22], the low hysteresis demonstrated in these  $\text{Mn}_3\text{Cu}_{1-x}\text{Sn}_x\text{N}$  samples results in reversible values of  $\Delta S_{\text{rev}}$  (figure 4(c)) and  $\Delta T_{\text{rev}}$  (figure 4(d)) being significantly larger.

Furthermore, we find significant reversible BCE even at pressures below 100 MPa due to the very low hysteresis, as demonstrated in figure 4(e) where  $\Delta T_{\text{rev}}$  for  $p = 80$  and  $140$  MPa are shown.  $\Delta T_{\text{rev}}$  peaks at  $\sim 1$  K and  $\sim 2$  K for those pressure values.

### 3.3. Discussion

We start by discussing the potential mechanisms underlying the low hysteresis of  $\text{Mn}_3\text{Cu}_{1-x}\text{Sn}_x\text{N}$ . It is useful to compare our results with other  $\text{Mn}_3\text{AN}$  and  $\text{Mn}_3(\text{A},\text{B})\text{N}$ . As has previously been demonstrated, the end-members ( $x = 0$  and  $x = 1$ ) of the series  $\text{Mn}_3\text{Cu}_{1-x}\text{Sn}_x\text{N}$  do not display a 1st-order magnetic transition and therefore no concomitant volume change occurs [14]. As  $x$  is increased above  $\sim 0.1$ , a sharp and large volume change occurs at the transition, which gradually weakens with increasing  $x$  although still remains until  $x = 0.7$  [14]. Consequently, one might also expect the hysteresis to decrease with increasing  $x$  in this manner. The measured values of the transition hysteresis for all samples are shown in figure 5(a). A reduction of  $\Delta T_{\text{hys}}$  is observed on increasing  $x$  from low values, reaching a minimum at  $x \sim 0.5$  and then increasing with further  $x$  doping. This suggests that  $\Delta T_{\text{hys}}$  is not simply linked to parameters related to the strength of the first-order transition, e.g. the magnitude of  $\Delta V/V$ ,  $dT/dp$  or  $\Delta S_{\text{t}}$  (see table 1). This behaviour is most apparent when plotting  $\Delta V/V$  and  $dT/dp$  against  $\Delta T_{\text{hys}}$ , as we show in figure 5(b). Here we can see that for  $\text{Mn}_3\text{AN}$ ,  $\Delta T_{\text{hys}}$  correlates extremely well with both  $\Delta V/V$  and  $dT/dp$ . In stark contrast is the behaviour of  $\text{Mn}_3\text{Cu}_{1-x}\text{Sn}_x\text{N}$ , where  $\Delta V/V$  and  $dT/dp$  are both comparable to those of  $\text{Mn}_3\text{GaN}$  and  $\text{Mn}_3\text{NiN}$ , yet  $\Delta T_{\text{hys}}$  is an order of magnitude smaller. Taken together these results suggest an additional mechanism underlies the  $x$ -dependence of  $\Delta T_{\text{hys}}$ , unrelated to the magnetovolume coupling. A similar type of hysteresis reduction as a function of composition has been shown in austenite/martensite systems, in which low hysteresis was linked to minimisation of strain between the austenite and martensite phases [30]. Unlike the austenite/martensite system however,  $\text{Mn}_3\text{Cu}_{1-x}\text{Sn}_x\text{N}$  does not undergo a change in lattice symmetry through the solid–solid phase transition. Nonetheless, it has been shown that Vegard’s law is not obeyed in  $\text{Mn}_3\text{Cu}_{1-x}\text{Sn}_x\text{N}$  system and an inflection is observed in the data for lattice constant as a function

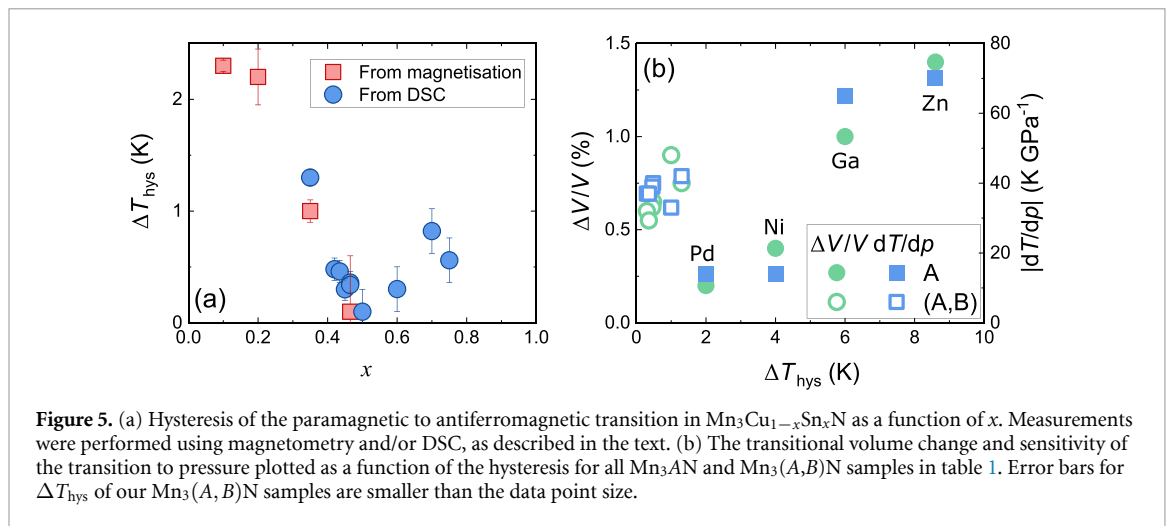


**Figure 5.** (a) Hysteresis of the paramagnetic to antiferromagnetic transition in  $\text{Mn}_3\text{Cu}_{1-x}\text{Sn}_x\text{N}$  as a function of  $x$ . Measurements were performed using magnetometry and/or DSC, as described in the text. (b) The transitional volume change and sensitivity of the transition to pressure plotted as a function of the hysteresis for all  $\text{Mn}_3\text{AN}$  and  $\text{Mn}_3(\text{A},\text{B})\text{N}$  samples in table 1. Error bars for  $\Delta T_{\text{hys}}$  of our  $\text{Mn}_3(\text{A},\text{B})\text{N}$  samples are smaller than the data point size.

of concentration,  $x$ , around  $x = 0.5$  [14]. It was argued that the cause of this was due to magnetic frustration suppressing spin fluctuations above  $T_{\text{N}}$  and therefore reducing the paramagnetic lattice volume. Thus, the magnetic frustration might assist the lattice contraction at  $T_{\text{N}}$ , facilitating the transition between the two states and therefore reducing the hysteresis. This could be seen as analogous to the strain related mechanism in the austenite/martensite systems. On a fundamental level, investigating the cause of the low hysteresis in  $\text{Mn}_3\text{Cu}_{1-x}\text{Sn}_x\text{N}$  should be of great interest in the broader context of magnetostructural materials, given that the transitions in many of the materials listed in table 1 are magnetostructural in origin (except  $\text{Ni}_{0.85}\text{Fe}_{0.15}\text{S}$ ) with largely similar transitional entropy changes.

We continue the discussion by comparing our results for the  $\text{Mn}_3\text{Cu}_{1-x}\text{Sn}_x\text{N}$  series with other metallic barocaloric materials. To do so, table 1 contains  $\Delta T_{\text{hys}}$  for  $A = \text{Ni}, \text{Ga}$  and  $\text{Zn}$  samples measured using the same method, in addition to several other metallic barocaloric systems obtained from recent reviews [1, 2]. From table 1 it is clear that  $\text{Mn}_3\text{Cu}_{1-x}\text{Sn}_x\text{N}$  materials display the smallest hysteresis among the metallic barocaloric systems studied so far. The only materials with  $\Delta T_{\text{hys}}$  of a similar order of magnitude are those of  $\text{Mn}_3\text{PdN}$  and  $\text{La}_{1.2}\text{Ce}_{0.8}\text{Fe}_{11}\text{Si}_2\text{H}_{1.86}$  from recent studies [22, 28]. In  $\text{Mn}_3\text{PdN}$ , reversible effects are also observed at 90 MPa with  $\Delta T_{\text{rev}} \sim 1$  K. Interestingly, for this pressure the absolute change of  $\Delta T_{\text{rev}}$  in our study is  $\sim 2$  K, however the peak is reduced due to the different thermal expansion properties away from the transition (see figure 4(c)). In  $\text{La}_{1.2}\text{Ce}_{0.8}\text{Fe}_{11}\text{Si}_2\text{H}_{1.86}$ , a key difference is that the hysteresis increases significantly with applied pressure. Nonetheless,  $\Delta T_{\text{rev}}$  peaks at 8 K for this material under 100 MPa, although a direct comparison is made difficult due to the use of direct methods (unlike the quasi-direct method used in the present study). However, it should be noted that the  $\text{Mn}_3\text{Cu}_{1-x}\text{Sn}_x\text{N}$  system has reversibility pressures as low as 20 MPa (based on the  $(T, p)$  phase diagram) for  $x = 0.42$  and  $0.435$ . This is significantly lower than other comparable metallic systems that we were able to identify in the literature.

In general, our results further demonstrate that significant reversible BCE can be achieved in metallic systems driven by moderate pressures of  $p < 100$  MPa. The extremely small hysteresis that can be engineered, combined with other properties such as high thermal conductivity, large density and chemical tunability, makes them attractive for potential applications. Specifically within the  $\text{Mn}_3(\text{A},\text{B})\text{N}$  family it has now been shown that the chemical flexibility allows the transition temperature, BCE and now the transition hysteresis to be tuned. However, only a small part of this chemical phase space has been explored and further improvements may be possible.

#### 4. Conclusions

Members of the antiperovskite series  $\text{Mn}_3\text{Cu}_{1-x}\text{Sn}_x\text{N}$  were synthesised with a range of different Sn concentrations to investigate their suitability as barocaloric materials. Key barocaloric parameters were extracted from these materials, demonstrating the sensitivity of both transition temperature and thermal hysteresis as a function of  $x$ . Furthermore, using high-pressure calorimetry, we demonstrated that these materials exhibit extremely small hysteresis ( $< 1$  K) and large BCE ( $> 20$  J K<sup>-1</sup> kg<sup>-1</sup>), under moderate pressures of  $p < 100$  MPa, making them more relevant for commercial purposes. By comparison to other undoped  $\text{Mn}_3\text{AN}$  antiperovskites, we propose that the small hysteresis is likely driven by a mechanism uncorrelated to the transitional volume change, and potentially due to strain matching across the transition. Furthermore, by investigating the microstructure using XRD and EBSD/EDS we are able to rule out

antiperovskite phase-inhomogeneity as the cause for the observed low hysteresis. As such, further work is under way to elucidate the mechanism driving low hysteresis in the  $\text{Mn}_3\text{Cu}_{1-x}\text{Sn}_x\text{N}$  antiperovskites.

## Data availability statement

All data that support the findings of this study are included within the article (and any supplementary files). Raw data associated with the figures can be found at <https://dx.doi.org/10.5525/gla.researchdata.1419>.

## Acknowledgment

This work was supported by MINECO Project No. PID2020-112975GB-I00 (Spain) and DGU Project No. 2021SGR-00343 (Catalonia). D B is grateful for support from a Leverhulme Trust Early Career Fellowship (No. ECF-2019-351) and a University of Glasgow Lord Kelvin Adam Smith Fellowship. We acknowledge Diamond Light Source for time on I11. M. Z. (CSC No. 202008310208) thanks the China Scholarship Council for funding.

## ORCID iDs


Frederic Rendell-Bhatti  <https://orcid.org/0000-0002-3470-786X>

Ming Zeng  <https://orcid.org/0000-0002-2697-2823>

Pol Lloveras  <https://orcid.org/0000-0003-4133-2223>

Josep-Lluís Tamarit  <https://orcid.org/0000-0002-7965-0000>

María Barrio  <https://orcid.org/0000-0003-3467-7581>

Eamonn T Connolly  <https://orcid.org/0000-0001-6103-3226>

Donald A MacLaren  <https://orcid.org/0000-0003-0641-686X>

Freya Johnson  <https://orcid.org/0000-0001-6922-3032>

David Boldrin  <https://orcid.org/0000-0003-3833-8341>

## References

- [1] Lloveras P and Tamarit J L 2021 Advances and obstacles in pressure-driven solid-state cooling: a review of barocaloric materials *MRS Energy Sustain.* **8** 3–15
- [2] Boldrin D 2021 Fantastic barocalorics and where to find them *Appl. Phys. Lett.* **118** 170502
- [3] Lloveras P et al 2019 Colossal barocaloric effects near room temperature in plastic crystals of neopentylglycol *Nat. Commun.* **10** 1803
- [4] Li B et al 2019 Colossal barocaloric effects in plastic crystals *Nature* **567** 506–10
- [5] Mañosa L, González-Alonso D, Planes A, Bonnot E, Barrio M, Tamarit J L, Aksoy S and Acet M 2010 Giant solid-state barocaloric effect in the Ni-Mn-In magnetic shape-memory alloy *Nat. Mater.* **9** 478–81
- [6] He X J, Xu K, Wei S X, Zhang Y L, Li Z and Jing C 2017 Barocaloric effect associated with magneto-structural transformation studied by an effectively indirect method for the  $\text{Ni}_{58.3}\text{Mn}_{17.1}\text{Ga}_{24.6}$  Heusler alloy *J. Mater. Sci.* **52** 2915–23
- [7] Stern-Taulats E et al 2015 Tailoring barocaloric and magnetocaloric properties in low-hysteresis magnetic shape memory alloys *Acta Mater.* **96** 324–32
- [8] Mañosa L, Stern-Taulats E, Planes A, Lloveras P, Barrio M, Tamarit J L, Emre B, Yüce S, Fabbri S and Albertini F 2014 Barocaloric effect in metamagnetic shape memory alloys *Phys. Status Solidi b* **251** 2114–9
- [9] Aznar A, Lloveras P, Kim J Y, Stern-Taulats E, Barrio M, Tamarit J L, Sánchez-Valdés C F, Sánchez Llamazares J L, Mathur N D and Moya X 2019 Giant and reversible inverse barocaloric effects near room temperature in ferromagnetic  $\text{MnCoGeB}_{0.03}$  *Adv. Mater.* **31** 1903577
- [10] Samanta T et al 2018 Barocaloric and magnetocaloric effects in  $(\text{MnNiSi})_{1-x}(\text{FeCoGe})_x$  *Appl. Phys. Lett.* **112** 021907
- [11] Matsunami D, Fujita A, Takenaka K and Kano M 2014 Giant barocaloric effect enhanced by the frustration of the antiferromagnetic phase in  $\text{Mn}_3\text{GaN}$  *Nat. Mater.* **14** 73–78
- [12] Boldrin D et al 2018 Multisite exchange-enhanced barocaloric response in  $\text{Mn}_3\text{NiN}$  *Phys. Rev. X* **8** 041035
- [13] Chi E O, Kim W S and Hur N H 2001 Nearly zero temperature coefficient of resistivity in antiperovskite compound  $\text{CuNMn}_3$  *Solid State Commun.* **120** 307–10
- [14] Takenaka K, Ichigo M, Hamada T, Ozawa A, Shibayama T, Inagaki T and Asano K 2014 Magnetovolume effects in manganese nitrides with antiperovskite structure *Sci. Technol. Adv. Mater.* **15** 15009–11
- [15] Mañosa L, González-Alonso D, Planes A, Barrio M, Tamarit J-L, Titov I S, Acet M, Bhattacharyya A and Majumdar S 2011 Inverse barocaloric effect in the giant magnetocaloric La-Fe-Si-Co compound *Nat. Commun.* **2** 595
- [16] Takenaka K, Ozawa A, Shibayama T, Kaneko N, Oe T and Urano C 2011 Extremely low temperature coefficient of resistance in antiperovskite  $\text{Mn}_3\text{Ag}_{1-x}\text{Cu}_x\text{N}$  *Appl. Phys. Lett.* **98** 022103
- [17] Wang C et al 2012 Tuning the range, magnitude and sign of the thermal expansion in intermetallic  $\text{Mn}_3(\text{Zn}, \text{M})_x\text{N}$  ( $\text{M} = \text{Ag}, \text{Ge}$ ) *Phys. Rev. B* **85** 220103(R)
- [18] Boldrin D et al 2021 Barocaloric properties of quaternary  $\text{Mn}_3(\text{Zn}, \text{In})\text{N}$  for room-temperature refrigeration applications *Phys. Rev. B* **104** 134104
- [19] Toby B H and Von Dreele R B 2013 GSAS-II: the genesis of a modern open-source all purpose crystallography software package *J. Appl. Crystallogr.* **46** 544–9
- [20] Aznar A, Lloveras P, Barrio M, Negrier P, Planes A, Mañosa L, Mathur N D, Moya X and Tamarit J-L 2020 Reversible and irreversible colossal barocaloric effects in plastic crystals *J. Mater. Chem. A* **8** 639–47



- [21] García J, Navarro R, Bartolomé J, Burriel R, González D and Fruchart D 1980 Specific heat of the cubic metallic perovskites  $\text{Mn}_3\text{ZnN}$  and  $\text{Mn}_3\text{GaN}$  *J. Magn. Magn. Mater.* **15–18** 1155–6
- [22] Tao K *et al* 2021 Giant reversible barocaloric effect with low hysteresis in antiperovskite  $\text{PdNMn}_3$  compound *Scr. Mater.* **203** 114049
- [23] Lin J *et al* 2020 Giant room-temperature barocaloric effect at the electronic phase transition in  $\text{Ni}_{1-x}\text{Fe}_x\text{S}$  *Mater. Horiz.* **7** 2690–5
- [24] Lloveras P, Samanta T, Barrio M, Dubenko I, Ali N, Tamarit J L and Stadler S 2019 Giant reversible barocaloric response of  $(\text{MnNiSi})_{1-x}(\text{FeCoGe})_x$  ( $x = 0.39, 0.40, 0.41$ ) *APL Mater.* **7** 061106
- [25] Wu R R *et al* 2015 Giant barocaloric effect in hexagonal  $\text{Ni}_2\text{In}$ -type Mn–Co–Ge–In compounds around room temperature *Sci. Rep.* **5** 18027
- [26] Stern-Taulats E, Planes A, Lloveras P, Barrio M, Tamarit J L, Pramanick S, Majumdar S, Frontera C and Mañosa L 2014 Barocaloric and magnetocaloric effects in  $\text{Fe}_{49}\text{Rh}_{51}$  *Phys. Rev. B* **89** 214105
- [27] Wei Z, Shen Y, Zhang Z, Guo J, Li B, Liu E, Zhang Z and Liu J 2020 Low-pressure-induced giant barocaloric effect in an all-d-metal Heusler  $\text{Ni}_{35.5}\text{Co}_{14.5}\text{Mn}_{35}\text{Ti}_{15}$  magnetic shape memory alloy *APL Mater.* **8** 051101
- [28] Liu Y, Zheng X, Liang F, Hu F, Huang Q, Li Z and Liu J 2022 Large barocaloric effect in intermetallic  $\text{La}_{1.2}\text{Ce}_{0.8}\text{Fe}_{11}\text{Si}_2\text{H}_{1.86}$  materials driven by low pressure *NPG Asia Mater.* **14** 30
- [29] Pérez-Reche F J, Vives E, Mañosa L and Planes A 2001 Athermal character of structural phase transitions *Phys. Rev. Lett.* **87** 195701
- [30] Cui J *et al* 2006 Combinatorial search of thermoelastic shape-memory alloys with extremely small hysteresis width *Nat. Mater.* **5** 286–90